Fusion-fission in nuclear systems with $40 \leq A_{CN} \leq 80$

S. J. Sanders
Department of Physics and Astronomy, The University of Kansas, Lawrence, Kansas 66045
(Received 5 August 1991)

The process of heavy-ion fusion followed by compound-nucleus fission is explored in the context of light nuclear systems. Spin- and mass-asymmetry-dependent saddle-point energies are calculated for several nuclei with $40 \leq A_{CN} \leq 80$ using the diffuse-surface, finite-nuclear-range model. A simple, double-spheroid approximation to the macroscopic-energy calculation is developed for determining fission barriers and fragment total kinetic energies. Fission cross sections are calculated within a statistical model and compared to experimental results. These comparisons support the idea that nuclear fission is the dominant process responsible for the fully energy-damped yields observed in this mass region.

I. INTRODUCTION

Nuclear-fission studies have tended to concentrate on relatively heavy systems of compound-nuclear mass $A_{CN} > 100$, largely ignoring the possibility of light-nucleus fission. Only recently has it been shown that compound-nucleus fission can also play an important role in heavy-ion reactions forming systems as light as $A_{CN} \sim 45-60$ [1–7]. The fission process in light systems has a number of distinctive features which set it apart from its heavier-system counterpart. In contrast to heavy-system fission, where symmetric breakup is favored in the absence of shell effects, the dependence of the macroscopic potential-energy surface on nuclear deformation and shape asymmetry favors the breakup of lighter systems into two unequal-mass fragments. This behavior emphasizes the progression from light-particle evaporation to heavy-fragment, binary breakup of the compound nucleus [8]. Another characteristic of light-nucleus fission is the relatively greater importance of the rotational energy in determining whether a given system will fission. For these systems it is only for the higher spin states of the compound nucleus that fission can compete favorably with light-particle (p-, n-, and α-particle) emission. At lower spin values the possibility of heavy-fragment emission is significantly reduced because of the rapid increase in the fission barrier in going to more symmetric breakup channels [2]. The limited range of spin values leading to fission suggests the possibility of using this process to learn more about the structure of nuclei at high spins.

Part of the difficulty in studying the fission of light systems has been the lack of model calculations to give guidance as to its system dependence and to highlight reactions where the measured binary-reaction yields are inconsistent with expectations. One of the motivations for the present work was to determine whether binary cross sections observed in several systems with $A_{CN} \cong 40$ and attributed to a dinuclear "orbiting" mechanism [9] are significantly in excess of what can be reasonably attributed to a fusion-fission process, as has been claimed [10]. For heavier systems the transition-state model [11], where the fission probability is related to the available phase space at the saddle point, has been quite successful in describing the general characteristics of the breakup process. The standard application of this model assumes a symmetric saddle-point configuration, however, and is therefore inappropriate for lighter systems. It is possible to generalize these calculations to include the possibility of fission to different mass fragments, as has been done for the ^{56}Ni system [2], but this requires calculation of the mass-asymmetric saddle-point energies—a lengthy procedure since it is essential in describing light-nucleus fission to include diffuse-surface and finite-nuclear-range effects [12] in calculating these energies. Earlier estimates of the fission-barrier energies based on the standard, lepodermous liquid-drop model led to barriers which were too large to allow for significant fission competition with light-particle emission. Realistic calculations of the fission process in light systems are only achieved by the inclusion of diffuse-surface and finite-nuclear-range corrections.

In this paper a simple parametrization is developed for the spin- and mass-asymmetry-dependent saddle-point energies in the mass range $40 \leq A_{CN} \leq 80$. This parametrization is fitted to saddle-point energies determined using the full macroscopic-energy calculation for the ^{40}Ca, ^{44}Ti, ^{49}V, ^{52}Fe, ^{56}Ni, and ^{80}Zr systems. The resulting parametrization is then incorporated into a statistical-model calculation using the transition-state model. Fission cross sections are calculated for heavy-ion reactions leading to the ^{40}Ca, ^{42}Sc, ^{47}V, ^{56}Ni, and ^{80}Zr compound systems and the results are compared to experimental, fully energy-damped, binary-reaction cross sections measured for these systems. The reactions considered are at energies where the complete-fusion process is expected to dominate over incomplete-fusion processes. In general, the experimentally observed cross sections throughout this mass range are found to be of a magnitude that can be explained by a fusion-fission mechanism assuming reasonable corrections to the saddle-point energies by shell effects in the nascent, relatively "cold" fission fragments.

This paper is organized as follows. In Sec. II the experimental evidence for fissionlike decay in the mass range $40 \leq A_{CN} \leq 80$ is briefly summarized. A simple parametrization of the fission barriers is presented in Sec. III, followed in Sec. IV by a discussion of how these barriers can be incorporated into a statistical-decay model. The calculated cross sections and final fragment kinetic energies for several representative systems are compared with experimental values in Sec. V. Results are summarized and conclusions stated in Sec. VI.

II. OVERVIEW OF EXPERIMENTAL SYSTEMATICS

The evidence for the fission of light nuclei stems from the observation of fully energy-damped, binary yields in heavy-ion reactions. These yields are characterized by constant $d\sigma/d\theta$ angular distributions, suggesting a decay from a rotating complex of lifetime comparable to, or greater than, the rotational period. The total kinetic energies of the outgoing fragments are independent of angle and can be accounted for with a simple model that considers the breakup of a rotating, binary system with no initial relative motion in the radial direction. The final kinetic energies are then given by summing the relative Coulomb, rotational, and nuclear potential energies in this configuration. These two features have led to the observed yields being characterized as resulting from either a dinucleus "orbiting" or fission mechanism. Table I summarizes some of the systems for which such yields have been observed, ordered by their compound nucleus mass A_{CN}, with $40 \leq A_{CN} \leq 80$.

Few of the experiments that show evidence for fissionlike processes in light systems are sufficiently complete to establish the exit-channel isotopic distributions or even the inclusive fission cross section. There are a number of reasons for this. In channels near the entrance channel, there can be significant quasielastic yields, requiring large-angle measurements covering a wide angular range to unravel the fully energy-damped products from those of faster processes. Further complicating the situation is the theoretical expectation that the fission process should favor the mass-asymmetric channels. In particular, for some of the light systems considered, the population of the ^{8}Be channel is expected to be significant. The experimental difficulties associated with ^{8}Be detection have so far prevented direct fission cross-section measurements in this channel. (Although Harmon *et al.* [13] have found evidence for this decay in the velocity distribution of the associated ^{32}S heavy recoil in the ^{28}Si+^{12}C reaction. The production of ground-state ^{8}Be fragments to large angles has also been deduced for the ^{32}S+^{24}Mg reaction by a measurement of the breakup α particles [2].) Depending on whether energy-loss or time-of-flight identification is employed, the current fission measurements tend to identify either the nuclear charge or mass of the reaction fragments, but not both. This complicates detailed comparisons of the isotopic distributions with calculations. In lighter systems with even, and equal, numbers of protons and neutrons, this last problem is mitigated by the observation that the channels corresponding to even-even $N=Z$ nuclei (i.e., ^{12}C, ^{16}O, ^{20}Ne, etc.) are the most strongly populated. Table I indicates the range of mass (or charge) which are presented in the various experimental references.

The secondary emission of light particles from the fission fragments can also pose a serious challenge for detailed comparisons of the theoretical and experimental mass-asymmetry dependence of the fission cross sections. One means of obtaining an experimental measure of the degree of secondary emission is to detect both fission fragments in coincidence, as has been done for the ^{56}Ni system [2]. In general, however, it is necessary to model the effects of secondary light-particle evaporation to compare calculations with experiment. A procedure for doing this, using the Monte Carlo evaporation code LILITA [14], is discussed in Sec. IV.

Another problem that arises in trying to compare calculated fission cross sections to experimental values is the need to know the fusion partial-wave distribution for the model calculations. These distributions are usually deduced from total fusion cross-section measurements by assuming a diffuse cutoff of the transmission coefficients for fusion. Unfortunately, there are relatively few cases where both evaporation-residue and fission cross sections are measured concurrently and analyzed in a consistent manner. Relatively small differences in the evaporation-residue cross sections used to deduce the total fusion cross section can lead to significant differences in the calculated fission competition. Also, the favoring of asymmetric-mass channels by the fission process can result in the evaporation-residue channels containing significant fission yields. To achieve a consistent analysis of a number of different systems, a simple critical-distance model is used in the present paper to estimate the total fusion cross section for each system considered. The sensitivity of the calculations to the assumed total fusion cross section is tested, however, in several cases where measured evaporation-residue cross sections are available.

TABLE I. Systems with $40 \leq A_{CN} \leq 80$ for which fissionlike yields have been reported.

Reaction	A_{CN}	$E_{c.m.}$ (MeV)	Reference	Detected fragments
^{28}Si+^{12}C	^{40}Ca	30–40	[9]	$5 \leq Z \leq 8$
^{28}Si+^{14}N	^{42}Sc	30–57	[31]	$5 \leq Z \leq 10$
^{35}Cl+^{12}C	^{47}V	46,51	[4,5]	$5 \leq Z \leq 12$
^{23}Na+^{24}Mg	^{47}V	46	[6]	$3 \leq Z \leq 10$
^{31}P+^{16}O	^{47}V	46	[7]	$6 \leq Z \leq 7$
^{37}Cl+^{12}C	^{49}V	37,44	[5]	$5 \leq Z \leq 11$
^{16}O+^{40}Ca	^{56}Ni	50–62	[47]	$22 \leq A \leq 36$
^{32}S+^{24}Mg	^{56}Ni	52,60	[1,2]	$12 \leq A \leq 28$
^{16}O+^{44}Ca	^{60}Ni	51–64	[47]	$22 \leq A \leq 36$
^{16}O+^{48}Ti	^{64}Zn	75	[48]	$5 \leq Z \leq 10$
^{28}Si+^{50}Cr	^{78}Sr	96	[43]	$12 \leq A \leq 58$
^{40}Ca+^{40}Ca	^{80}Zr	86,103	[24,43]	$6 \leq A \leq 62$

III. ASYMMETRIC FISSION BARRIERS

The application of the transition-state model in light nuclear systems requires knowing the macroscopic-

energy fission barriers as functions of the spins and mass asymmetries of the respective decay channels. For light systems it is important that these calculation include diffuse-surface and finite-nuclear-range effects. Although the procedure for calculating these barriers using the Yukawa-plus-exponential model [15] is discussed by Sierk [12] and an interpolation routine is available for finding the mass-symmetric barriers for nuclei of atomic number $Z \geq 20$ [16], the mass-asymmetric barriers are not readily available. The full calculation of the fission saddle-point energy for a specific mass asymmetry and spin of a compound nucleus is sufficiently involved to make it impractical to directly incorporate these calculations within a statistical-model calculation. Fortunately, the macroscopic fission barrier is a smoothly varying function of spin and mass asymmetry, making a simple parametrization of the barrier energies possible.

To develop this parametrization, the saddle-point energies for several nuclei in the mass range $40 \leq A_{CN} \leq 80$ were first calculated following the procedures outlined in Ref. [12]. These full calculations were done for the ^{40}Ca, ^{44}Ti, ^{49}V, ^{52}Fe, ^{56}Ni, and ^{80}Zr systems. Saddle-point energies were found by determining the stationary points of the compound-nucleus potential-energy surface as a function of spin and constrained mass asymmetry. The potential-energy calculations, in which the shape of the compound nucleus is expressed in terms of three connected quadratic surfaces of revolution, include diffuse-surface and finite-nuclear-range effects. The parameters used for the potential calculation were the same as given in Ref. [12].

The shape parametrization, discussed by Nix in Ref. [17], can be written in cylindrical coordinates (see Fig. 1) as

$$\rho^2 = \begin{cases} b_1^2 - (b_1^2/a_1^2)(z-l_1)^2 & \text{for } l_1 - a_1 \leq z \leq z_1 \ , \\ b_2^2 - (b_2^2/a_2^2)(z-l_2)^2 & \text{for } z_2 \leq z \leq l_2 + a_2 \ , \\ b_3^2 - (b_3^2/a_3^2)(z-l_3)^2 & \text{for } z_1 \leq z \leq z_2 \ , \end{cases}$$

where a_3 is imaginary for light nuclei with constricted necks at the saddle point (as is the case in Fig. 1). Constraints on the shape coordinates assure that the nuclear surface is continuous with smooth transitions between the three segments. With these constraints the shape is determined by five nontrivial coordinates. Although restrictive, this parametrization is well behaved in the procedure for locating the saddle points. Sierk [12] has shown that more general parametrizations can lead to unrealistic shapes for lighter systems, with two saddle points for nuclei with $Z \leq 50$.

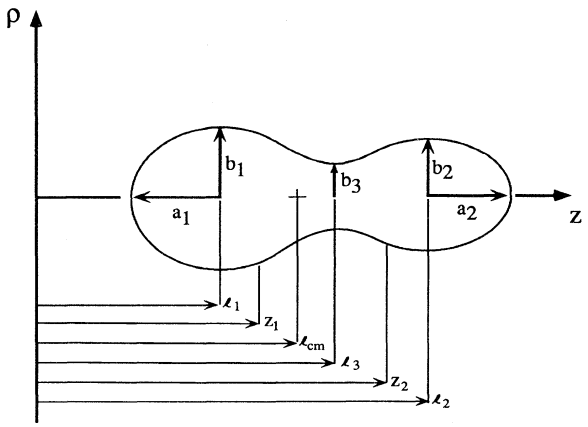

FIG. 1. Geometry of saddle-point shapes consisting of three connected quadratic surfaces of revolution.

The saddle-point energies were calculated for all even spins ranging from $0.4J_{max}$ to J_{max} for the respective compound nuclei, where J_{max} is the spin value for which the mass-symmetric fission barrier vanishes. Only a few calculations were done for lower spin values since these play little or no role in the fission process. (The final parametrization was, however, found to reproduce these results reasonably well). The program used for these calculations was checked against the results of Sierk for the symmetric barriers in the mass range $40 \leq A_{CN} \leq 80$, always agreeing to better than 0.5 MeV, and by comparing with the asymmetric barrier calculations published for the spinless ^{111}In system by Sierk [18], again with better than 0.5-MeV agreement for all mass asymmetries.

The minimization procedure used in these calculations was generally successful in finding suitable saddle-point configurations for mass asymmetries $\eta < 0.45$, with $\eta = 1 - 2(A_L/A_{CN})$. A_L refers to the mass of the lighter fission fragment assuming the final mass ratio is the same as the ratio of volumes on the two sides of the constricted neck at the saddle point. It was not always possible to converge on a valid saddle-point configuration for more asymmetric mass divisions, and in these cases it was necessary in calculating the fission cross sections to rely on extrapolated barrier energies based on the double-spheroid approximation, to be discussed next, developed from the more symmetric barriers.

The saddle-point energies obtained with the full calculations were fitted by a double-spheroid approximation in order to obtain a simple method of calculating these energies. The model is of two, axially aligned, ellipsoidally deformed spheroids separated by a gap. The goal was to obtain a reasonable scaling for the saddle-point energies rather than attempting to reproduce the full saddle-point calculations. In this double-spheroid model, the saddle-point energy is given by

$$V_{saddle}(J_{CN}, \eta) = V_C + V_r + V_n + V_0 \ ,$$

where V_C, V_r, and V_n are the Coulomb, rotational, and nuclear energies, respectively, and V_0 is an energy offset.

In obtaining expressions for the different components of V_{saddle}, it is found convenient to express V_r in terms of an ellipsoidal geometry, the geometry used for the double-spheroid approximation, whereas V_C and V_n are most readily expressed in terms of a quadrupoloid geometry. It is therefore necessary to have a way of equating these two geometries. For a spheroid of mass A, the equivalent quadrupoloid to the ellipsoidal shape of semiminor to semimajor axis ratio b/a is taken to have deformation

$$\beta_0 = \frac{2}{Y_{2,0}(0,0)} \frac{1-b/a}{1+2b/a} .$$

The semimajor axis length a of the ellipsoid is expressed in terms of the spherical radius R, with $R = r_0 A^{1/3}$ and $a = R(b/a)^{-2/3}$. The comparable semimajor axis length for the quadrupoloid $\bar{a}$ is given by $\bar{a} = \tilde{R}[1 + \frac{1}{2}\sqrt{(5/\pi)}\beta_0]$, where $\tilde{R}$ is a scaled radius such that the equivalent quadrupoloid has the same volume as the ellipsoid used for the double-spheriod approximation. For spherical shapes, $R = \tilde{R}$. The distance between centers r in the double-spheroid approximation is given by $r = s + a_1 + a_2$, where s is the gap distance between the ellipsoidal surfaces. When using the equivalent quadrupoloid shapes, the gap distance was taken as $\bar{s}$ with $\bar{s} = r - \bar{a}_1 - \bar{a}_2$. The ellipsoidal and quadrupoloid geometries are sufficiently similar at the deformations encountered in this analysis that the corresponding distances are very similar.

The two-body potential of Krappe, Nix, and Sierk [19] was used to determine the nuclear interaction. This potential is based on the same Yukawa-plus-exponential, finite-range model utilized in deriving the saddle-point energies. The interaction potential for two nuclei of radii $\tilde{R}_1$ and $\tilde{R}_2$ and quadruple deformations $\beta_{0,1}$ and $\beta_{0,2}$, respectively, has the form [19]

$$V_n = -D\left[F + \frac{\bar{s}}{a}\right]\frac{\tilde{R}_{12}}{r} e^{-\bar{s}/a} - 4\frac{c_s'}{a r_0^2}[\beta_{0,1}\tilde{R}_1^3 \mathcal{A}_2(1) + \beta_{0,2}\tilde{R}_2^3 \mathcal{A}_2(2)] Y_{2,0}(0,0) ,$$

where $\tilde{R}_{12} = \tilde{R}_1 + \tilde{R}_2$ and $Y_{2,0}(0,0)$ is the spherical harmonic evaluated at $\theta = 0°$ and $\phi = 0°$. The depth constant D and constant F are given by

$$D = \frac{4a^3 g(\tilde{R}_1/a) g(\tilde{R}_2/a) e^{-\tilde{R}_{12}/a}}{r_0^2 \tilde{R}_{12}} c_s'$$

and

$$F = 4 + \frac{\tilde{R}_{12}}{a} - \frac{f(\tilde{R}_1/a)}{g(\tilde{R}_1/a)} - \frac{f(\tilde{R}_2/a)}{g(\tilde{R}_2/a)} ,$$

respectively, with $g(x) = x\cosh(x) - \sinh(x)$ and $f(x) = x^2 \sinh(x)$. The geometric mean of the surface energies of the interacting particles is used with

$$c_s' = [c_s(1) c_s(2)]^{1/2} .$$

The individual effective surface-energy constants depend on the relative neutron-proton excess $I_i = (N_i - Z_i)/A_i$ $(i = 1,2)$ with $c_s(i) = a_s(1 - \kappa_s I_i^2)$, where a_s is the surface-energy constant and κ_s is the surface-asymmetry constant. For consistency with the macroscopic-energy calculations, the constants used for these calculations were $r_0 = 1.16$ fm, $a = 0.68$ fm, $a_s = 21.13$ MeV, and $\kappa_s = 2.3$.

The deformation dependence is expressed with the functions $\mathcal{A}_2(1)$ and $\mathcal{A}_2(2)$ for particles 1 and 2, respectively. For particle 1(2) with quadrupole deformation $\beta_{0,1(2)}$, this term is written as

$$\mathcal{A}_2(1(2)) = a\frac{\partial}{\partial a}\left\{ g\left[\frac{\tilde{R}_{1(2)}}{a}\right]\left\{\left[\frac{a}{\tilde{R}_{2(1)}} + 3\left[\frac{a}{\tilde{R}_{2(1)}}\right]^3\right]\sinh\left[\frac{\tilde{R}_{2(1)}}{a}\right] - 3\left[\frac{a}{\tilde{R}_{2(1)}}\right]^2\cosh\left[\frac{\tilde{R}_{2(1)}}{a}\right]\right\} \times \left[\frac{a}{r} + 3\left[\frac{a}{r}\right]^2 + 3\left[\frac{a}{r}\right]^3\right] e^{-r/a} \right\} .$$

The form given above for the nuclear potential is only valid for $\bar{s} \geq 0$. Although a generalization of the potential for $\bar{s} < 0$ is possible, as discussed in Ref. [19], this was not needed for the present work.

The rotational-energy term was taken as

$$V_r = \frac{\hbar^2}{2\mathcal{I}_{tot}} J_{CN}(J_{CN}+1) ,$$

with

$$\mathcal{I}_{tot} = \mathcal{I}_1 + \mathcal{I}_2 + \mathcal{I}_{rel}$$

and

$$\mathcal{I}_{1(2)} = 0.2 A_{1(2)} R_{1(2)}^2 [(b/a)^{2/3} + (b/a)^{-4/3}] + 4 A_{1(2)} a_{Yukawa}^2 ,$$

$$\mathcal{I}_{rel} = \mu r^2 .$$

A_1 and A_2 refer to the atomic masses of the two fragments, respectively. The surface-diffuseness parametric $a_{Yukawa} = 0.75$ fm. The radii R_1 and R_2 are for the ellipsoidal shape.

The expression used for the Coulomb energy between the two deformed spheroids again makes use of the equivalent quadrupoloid shapes with [20]

$$V_C = \frac{Z_1 Z_2 e^2}{r}\left[1 + \frac{3}{5}\frac{Y_{2,0}(0,0)}{r^2}(\beta_{0,1}\tilde{R}_1^2 + \beta_{0,2}\tilde{R}_2^2)\right] .$$

The charge was assumed to be uniformly distributed with $Z_1 = Z_{CN} A_1 / A_{CN}$.

Simple functional forms for the double-spheroid parameters can be found which make it possible to use this model to quickly and accurately estimate saddle-point energies in the mass range $40 \leq A_{CN} \leq 80$. These energies

would otherwise have to determined through the full macroscopic-energy calculations. The surface separation s is taken to have the functional form $s(\text{fm})=0.79+0.00805A_{\text{CN}}$, with the coefficients determined by fitting the results of the full calculation. The ratio of minor to major axis lengths b/a is taken as 0.8 for both spheroids. The energy offset is taken as

$$V_0(\text{MeV})=-5.19+0.0046A_{\text{CN}}+E_{\text{sphere}}(A_1)+E_{\text{sphere}}(A_2)-E_{\text{sphere}}(A_{\text{CN}}) .$$

E_{sphere} is the macroscopic energy of a spherical nucleus and is given by Eq. (2) of Ref. [21], assuming a uniform charge to mass distribution between the two fragments. For this calculation the pairing and Wigner energy terms are set to zero. Incorporating this potential-energy difference has the advantage of including a charge-asymmetry term in the overall barrier energies, allowing for a parametrization that works for even-odd and odd-odd nuclei as well as the even-even nuclei. The expression for V_0 also contains an expression linear in the compound-nucleus mass.

A comparison is made between the double-spheroid approximation using fitted parameters (solid curves) and the full macroscopic-energy calculations (points) for several systems in Fig. 2. For the ^{40}Ca, ^{44}Ti, ^{49}V, ^{52}Fe, and ^{56}Ni systems, the comparison is shown for the two spin values corresponding to $0.6J_{\text{max}}$ and $0.8J_{\text{max}}$, respectively. The comparison is shown at $0.64J_{\text{max}}$ and $0.93J_{\text{max}}$ for the heavier ^{80}Zr system. In each case the two spin values cover the region where fission competition is likely to be significant. The calculated barrier energies, based on the double-spheroid model, are extrapolated to the mass asymmetry corresponding to a lighter fragment mass of $A_L=6$. The Sierk value [12] for the symmetric saddle-point energy is shown to the left of each line, indicating good agreement with the present calculations. The limiting case of $\eta=1$, where the lighter-fragment mass vanishes, should be the same as the equilibrium energy of the nucleus at the corresponding spin value. These equilibrium values, tabulated by Sierk, are also shown. The energy difference between the saddle point and corresponding equilibrium energies at a given spin value is the fission barrier B_f.

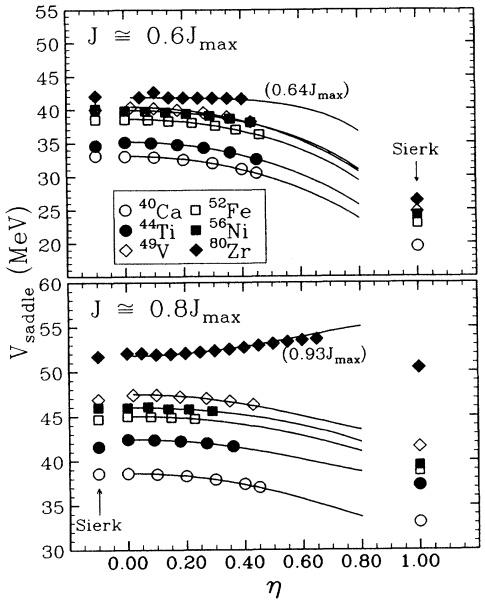

FIG. 2. Fission barrier energies as a function of mass asymmetry for the ^{40}Ca, ^{44}Ti, ^{49}V, ^{52}Fe, ^{56}Ni, and ^{80}Zr systems. Spin values corresponding to $0.6J_{\text{max}}$ and $0.8J_{\text{max}}$ are shown for all but the ^{80}Zr systems, with $J_{\text{max}}=30\hbar$, $36\hbar$, $41\hbar$, $42\hbar$, and $43\hbar$ for the five systems, respectively. For ^{80}Zr spins, $36\hbar$ ($0.64J_{\text{max}}$) and $52\hbar$ ($0.93J_{\text{max}}$) are shown. The symbols indicate values obtained from the full saddle-point calculations, while the curves are for the double-spheroid parametrization discussed in the text. The results at $\eta=1.0$ are from the equilibrium energy calculations of Sierk [12]. The Sierk values for the symmetric barrier energies are shown to the left of the curves.

TABLE II. Selected examples of double-spheroid parametrization.

Z_{CN}	A_{CN}	A_1	η	J	J_{max}	s (fm)	b/a	V_C (MeV)	V_r (MeV)	V_n (MeV)	V_0 (MeV)	E_K^{tot} (MeV)
20	40	12	0.40	$18\hbar$	$30\hbar$	1.11	0.8	15.1	8.3	−2.8	10.3	18.1
		20	0.00					17.7	7.3	−3.0	11.0	20.2
		12	0.40	24				15.1	14.6	−2.8	10.3	22.4
		20	0.00					17.7	12.9	−3.0	11.0	24.3
23	49	12	0.51	24	41	1.18	0.8	16.7	11.5	−2.7	11.3	21.6
		24	0.02					21.9	9.3	−2.9	12.2	25.9
		12	0.51	32				16.7	20.3	−2.7	11.3	27.2
		24	0.02					21.9	16.4	−2.9	12.2	31.1
28	56	12	0.57	26	43	1.24	0.8	21.7	11.6	−2.6	5.4	26.4
		28	0.00					31.0	8.8	−2.9	3.1	34.7
		12	0.57	34				21.7	19.6	−2.6	5.4	31.4
		28	0.00					31.0	14.9	−2.9	3.1	39.2
40	80	16	0.60	36	56	1.43	0.8	37.4	12.8	−2.3	−7.6	43.1
		40	0.00					56.0	9.3	−2.6	−20.8	60.5
		16	0.60	52				37.4	26.4	−2.3	−7.6	51.4
		40	0.00					56.0	19.2	−2.6	−20.8	51.8

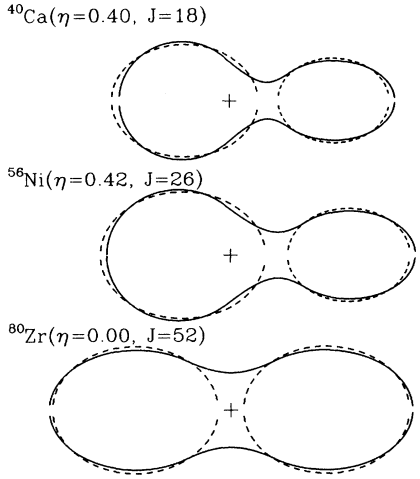

FIG. 3. Comparison of shapes determined from the full saddle-point calculations (solid curves) and the double-spheroid parametrization of the saddle-point energies (dashed curves). The $\eta=0.40$ and 0.42 asymmetries for ^{40}Ca and ^{56}Ni correspond to $A_1/A_2=12/28$ and 16/40, respectively.

Table II gives typical shapes and potential-energy values calculated in the double-spheroid approximation. Figure 3 compares the shapes of the double-spheroid approximation to the connected-quadratic-surface approximation used in the saddle-point calculations for several systems. The resulting configurations are similar to those of the "exact" saddle-point calculations, although clearly with differences. The spheroid approximation does not show a neck connecting the two fragments, and the assumption of equal fragment deformation is an oversimplification. The approximation is sufficiently similar in geometry to the calculated saddle-point shapes, however, to expect that the relative rotational and Coulomb energy between the two fragments will be reproduced reasonably well. This can be tested by comparing the calculated fragment total kinetic energy $E_K^{\rm tot}$ predicted by the double-spheroid approximation with experimental values. For these comparisons the total kinetic energy in the exit channel is taken as

$$E_K^{\rm tot}=V_C+V_n+\frac{\hbar^2}{2\mathcal{I}_{\rm rel}}l(l+1)\ ,$$

with

$$l=\frac{\mathcal{I}_{\rm rel}}{\mathcal{I}_{\rm tot}}J_{\rm CN}\ .$$

Although the saddle and scission points in light systems are expected to be quite similar [22], any dissipative process active between these configurations will result in somewhat lower fragment kinetic energies.

IV. TRANSITION-STATE MODEL CALCULATIONS

Fission cross sections were calculated using the transition-state model [11], with the fission probability taken as being proportional to the available phase space at the saddle point. In heavier systems the level density above the symmetric saddle point is generally used in these calculations. This is justified by a mass-asymmetry dependence of the saddle-point energy which favors symmetric fission. In contrast, the macroscopic energy in light systems favors the asymmetric breakup of the compound nucleus, requiring that the spin-dependent, mass-asymmetric saddle-point energies be used to determine the fission phase space. In this section the details of fission calculations based on the asymmetric-mass barriers are given.

A. Fusion partial-wave distributions

The fusion cross-section calculations consist of determining the compound-nucleus spin distribution. For these calculations the fusion partial cross sections for formation of a compound nucleus of spin J from projectile and target nuclei of spins J_p and J_t, respectively, at center-of-mass energy E were taken as [23]

$$\sigma_J=\pi\lambda\!\!\!^{-2}\frac{2J+1}{(2J_p+1)(2J_t+1)}\sum_{S=|J_p-J_t|}^{J_p+J_t}\sum_{l=|J-S|}^{J+S}T_l(E)\ ,$$

with

$$T_l(E)=\frac{1}{1+\exp\{[l-l_0(E)]/\Delta\}}\ .$$

The total fusion cross section $\sigma_{\rm fus}^{\rm tot}$ is then given by

$$\sigma_{\rm fus}^{\rm tot}=\sum_{J=0}^{\infty}\sigma_J\ .$$

The diffuseness parameter Δ was set to $1\hbar$. Although this parameter is, in principal, system dependent, for the present survey of the fission process in light systems it was held fixed so as not to introduce an arbitrary, system-dependent constant in the comparison of the theoretical to experimental results.

The energy-dependent, critical angular momentum for fusion $l_0(E)$ was set to the maximum partial wave for which the nuclear surfaces of the target and projectile (assumed spherical) touch, subject to the interaction potential $V_{\rm int}$ in the entrance channel. This potential is given by

$$V_{\rm int}=\frac{Z_pZ_te^2}{r}+\frac{\hbar^2}{2\mu r^2}l(l+1)+V_n\ ,$$

where Z_p and Z_t are the charges of the projectile and target nuclei, respectively, l is the angular momentum brought into the reaction, and r is the distance between the two nuclear centers. The potential of Krappe *et al.* [19] was again used for the nuclear interaction V_n, however, assuming spherical shapes for the target and projectile. This form for $V_{\rm int}$ assumes a "self-masking dissipation" [24] where the frictional energy loss from the relative motion in the entrance channel comes entirely from the centrifugal energy as the orbital angular momentum decreases.

An alternative method of determining l_0 is to use the

experimental total fusion cross section $\sigma_{\rm fus}^{\rm tot}$ to deduce this quantity. This requires, however, knowing both the total evaporation residue and fission cross sections. In several cases where this information was available, the fission calculations were also made using the experimentally deduced l_0 values.

B. $\Gamma_f/\Gamma_{\rm tot}$

The ratio of the fission decay width Γ_f to the total decay width of the compound nucleus $\Gamma_{\rm tot}$ was determined using the statistical model. It was assumed that the compound nucleus decays through the emission of neutrons, protons, alphas particles, or fission fragments, with

$$\Gamma_{\rm tot}=\Gamma_n+\Gamma_p+\Gamma_\alpha+\Gamma_f \ .$$

The fission partial width Γ_f can be further expressed as a sum over the possible heavy-fragment decay channels. To reduce the length of the calculations, this sum was truncated with

$$\Gamma_f=\sum_{A_L=6}^{A_{\rm CN}/2}\sum_{Z_L=A_L/2-2}^{A_L/2+2}\Gamma_f(Z_L,A_L) \ ,$$

where $\Gamma_f(Z_L,A_L)$ is the decay width to the channel where the lighter fragment has charge Z_L and mass A_L. For odd compound-nucleus masses, the upper limit of the atomic-mass summation was taken to be $(A_{\rm CN}-1)/2$, and for odd values for the light-fragment mass, the corresponding charge sum was taken over ± 2 units about the central charge of $(A_L+1)/2$. Although a summation is performed over the different fragment charges, the results are not significantly changed if only the most probable (lowest barrier) channel is considered for each mass asymmetry. For the light systems and corresponding bombarding energies discussed here, secondary fission following light-particle emission from the compound nucleus is unlikely. This is a consequence of the limited spin range over which the fission process competes with light-particle emission. It is therefore sufficient in calculating fission cross sections to use energy-integrated widths for the compound-nucleus decay, without following the full decay chain.

The partial widths for the three light particles x ($x=n$, p, or α) of spin s_x to be emitted from the compound nucleus of excitation energy $E_{\rm CN}^*$ and spin $J_{\rm CN}$ to form an evaporation-residue nucleus ER of excitation energy $E_{\rm ER}^*$ and spin $J_{\rm ER}$ are given by [23,25]

$$\Gamma_x=\int\frac{\rho_{\rm ER}(E_{\rm ER}^*-\Delta,J_{\rm ER})}{2\pi\hbar\rho_{\rm CN}(E_{\rm ER}^*-\Delta,J_{\rm ER})}\times\sum_{S=|J_{\rm ER}-s_x|}^{J_{\rm ER}+s_x}\sum_{l=|J_{\rm CN}-s|}^{J_{\rm CN}+s}T_l^x(\varepsilon_x)d\varepsilon_x \ ,$$

where the integral is over all kinetic energies of the emitted light particle ε_x, and $\rho_{\rm CN}$ and $\rho_{\rm ER}$ are the level densities of the compound nucleus and resulting evaporation residue, respectively. The transmission coefficients $T_l^x(\varepsilon_x)$ are obtained from optical-model calculations using average parameters.

The parameter Δ determines the zero point of the effective excitation energy. Since fission comes early in the decay chain, the densities corresponding to relatively high excitation energies in the compound nucleus and residues dominate the partial-width calculations. At these high energies Δ can be determined by assuming that the virtual ground state for the level densities should correspond to the macroscopic-energy ground state [23], with

$$\Delta({\rm MeV})=E_B(Z,A)-E_B^{\rm macro}(Z,A) \ .$$

E_B is the measured binding energy of the nucleus, and $E_B^{\rm macro}$ is the corresponding macroscopic energy, obtained using the binding energy terms from Eq. (2) of Ref. [21], and including the Wigner energy term, but not the pairing energy.

The fission widths $\Gamma(Z_L,A_L)$ are obtained with an expression similar to that for the light-fragment widths, but using the level density above the mass-asymmetry-dependent saddle point:

$$\Gamma_f(Z_L,A_L)=\int_{\varepsilon=0}^{20\ {\rm MeV}}\frac{\rho_f(E_{\rm CN}^*-V_{\rm saddle}(J_{\rm CN},\eta)-\Delta V_{\rm shell}(J_{\rm CN},Z_L,A_L)-\Delta-\varepsilon,J_{\rm CN})}{2\pi\hbar\rho_{\rm CN}(E_{\rm CN}^*-\Delta,J_{\rm CN})}T_{f_{\rm CN}}^f(\varepsilon)d\varepsilon \ ,$$

where

$$T_{f_{\rm CN}}^f(\varepsilon)=\begin{cases}1 & \text{for } \varepsilon\le E_{\rm CN}^*-V_{\rm saddle}(J_{\rm CN},\eta)-\Delta V_{\rm shell}(Z_L,A_L)-\Delta \ ,\\ 0 & \text{for } \varepsilon>E_{\rm CN}^*-V_{\rm saddle}(J_{\rm CN},\eta)-\Delta V_{\rm shell}(Z_L,A_L)-\Delta \ .\end{cases}$$

The integration variable ε can be envisioned as the energy going into internal excitation of the system at the saddle point. Limiting this variable to 20 MeV, even when the energetics would allow for a greater value, does not significantly affect the width calculations since the level density is strongly energy dependent. $V_{\rm saddle}(J_{\rm CN},\eta)$ is the spin- and mass-asymmetry-dependent saddle-point energy with respect to the macroscopic-energy ground state of the compound nucleus, as discussed in the previous section. This is a smoothly varying function of the mass asymmetry η, as seen in Fig. 2.

The experimental evidence indicates a strong isotopic dependence for the fission cross sections that is inconsistent with a smooth dependence of the potential-energy surface on the mass-asymmetry parameter η. This can be understood in terms of shell and pairing corrections to

the energy surface from the structure of a nascent fission fragments. As a first approximation of these corrections, a term $\Delta V_{\text{shell}}(Z_L, A_L)$ has been added to the barrier energy. This term, which can be viewed as a macroscopic shell correction, consists of the sum of the Wigner energy corrections [21] for the two nascent fragments, with

$$\Delta V_{\text{shell}}(Z_L, A_L) = W(Z_L, A_L) + W(Z_{CN} - Z_L, A_{CN} - A_L)$$

and

$$W(Z, A) = (36 \text{ MeV}) \left| \left| \frac{A-2Z}{A} \right| + \begin{cases} 1/A, & Z \text{ and } N \text{ odd and equal} \\ 0, & \text{otherwise} \end{cases} \right| .$$

It follows from the form of the Wigner energy that, for compound nuclei where the neutron and proton numbers are equal, the total barrier energy $V_{\text{saddle}} + \Delta V_{\text{shell}}$ will have local minima for channels where both fragments also have $N=Z$ and for which $\Delta V_{\text{shell}} = 0$. Until more realistic calculations of the shell and pairing corrections are performed for the strongly deformed, nascent fission fragments, detailed agreement between the calculated and experimental isotope distributions cannot be expected. It will be shown in the next section, however, that the simple expression for ΔV_{shell} presented here is sufficient to reproduce the general trends of the experimental results.

The model calculation also requires level densities for the light-particle evaporation residues and at the saddle point (the level density of the compound nucleus is common to all of the widths and, consequently, does not affect the different branching ratios). The same Fermi-gas formula [26] was used to determine both the evaporation residues and fission saddle-point densities, with

$$\rho(u, J) = \frac{2J+1}{12} \sqrt{a_x} \left[\frac{\hbar^2}{2\mathcal{J}} \right]^{3/2} [u]^{-2} \exp(2\sqrt{a_x u})$$

and

$$u = \begin{cases} E^*_{\text{ER}} - \dfrac{\hbar^2}{2\mathcal{J}} J(J+1) - \Delta, & \text{evaporation residues} , \\ E^*_{\text{CN}} - V(J_{\text{CN}}, \eta) - \Delta V_{\text{shell}}(Z_L, A_L) - \Delta - \epsilon, & \text{saddle point} . \end{cases}$$

For the evaporation residues, the level-density parameter $a_x = a_n$, and the spin is that of the evaporation residue $J = J_{\text{ER}}$. The saddle-point densities are calculated with $a_x = a_f$ and $J = J_{\text{CN}}$. The moment of inertia coefficients for the evaporation residues was obtained using the equilibrium energies calculated by Sierk [12], with

$$\frac{\hbar^2}{2\mathcal{J}} = \frac{E_{\text{yrast}}(J)}{J(J+1)} ,$$

and taking the limiting value of this expression for $J=0$. Again, the saddle-point moments of inertia and energies are calculated using the double-spheroid approximation.

The extent to which fission competes with light-particle evaporation is largely determined by the relative values of level-density parameters a_n and a_f. In heavier systems it has been found that fission competition can be reliably reproduced by setting $a_n = a_f$ if fission barriers calculated with the Yukawa-plus-exponential model are used. A similar assumption is employed in the present calculations where values of $a_n = A_{\text{ER}}/(8.0 \text{ MeV})$ and $a_f = A_{\text{CN}}/(8.0 \text{ MeV})$ are assumed.

C. Comparison with other models

Previous models developed to describe fissionlike processes in light nuclear systems include the equilibrium model of orbiting of Shivakumar *et al.* [27,28] and the extended Hauser-Feshbach model of Matsuse and Lee [29,30]. These models, together with the transition-state picture, share the common idea that the final fragment distribution is determined by statistical processes. Otherwise, the premise of the equilibrium model is quite different from either the transition-state picture or the extended Hauser-Feshbach model. Both the transition-state and extended Hauser-Feshbach models describe a fusion-fission process.

The equilibrium model gives a unified description of fusion and damped binary-fragment yields by viewing the dinuclear orbiting configuration as a doorway which can lead to fusion or binary decay. In this picture the final mass and energy distributions of the heavy fragments are determined after the dinuclear complex has held together long enough for the relevant degrees of freedom to reach equilibrium. This is a statistical model in that the relative probability of fusion to binary decay is determined by the density of states in the respective configurations. However, unlike fusion-fission models, the binary yields arise from a configuration that never achieves the compact form of the equilibrated compound nucleus. This model is successful in describing both the evaporation-residue and damped binary yields, as well as fragment total kinetic energies, for several systems in the mass $A=40$ region [28,31,32] and, by allowing for fragment deformation, can also successfully describe the observed yields from the $^{32}S + ^{24}Mg$ reaction [2]. As a predictive tool, however, the model suffers from requiring system-dependent changes in the nuclear-strength parameter and fragment deformations to achieve good reproduction of

experimental results, without giving guidance as to how these parameters should be changed. For nearby systems, however, it can be expected that these changes will be small.

The extended Hauser-Feshbach model starts with the same premise as the transition-state picture that the fully energy-damped, binary fragment yields arise from the process of complete fusion followed by binary fission. The two models principally differ in how the phase space for the fission process is determined: The extended Hauser-Feshbach model takes this as a product of the level densities in the two nascent fragments, at the point of scission. The effective Q values for the different mass channels, used for the level-density calculations, are varied between their asymptotic values (calculated with ground-state binding energies) and the liquid-drop value where shell effects vanish. Although this model is similar in concept to the scission-point model developed to describe heavier-system fission [33], the significant energy differences between the saddle and scission points found in heavier systems are not expected to be present in light systems [22]. This suggests that the predictions of the extended Hauser-Feshbach and transition-state models might be expected to be similar. The advantage of the transition-state picture, however, is that the geometry of the saddle point, including the role of fragment deformation, is fully determined by the macroscopic-energy calculations. In the extended Hauser-Feshbach model, a fragment-separation parameter is adjusted in an *ad hoc* manner to account for the system-dependent geometry.

D. Correction for secondary light-particle emission

For most of the reactions being considered, the possibility exists for the fission fragments to be emitted with excitation energies above their respective particle-emission thresholds. The resulting secondary light-particle emissions can strongly affect the measured mass distribution of the fragments. In the case of the $^{32}S+^{24}Mg$ reaction, for instance, where a coincidence measurement enabled an experimental correction to be made for this evaporation, it was found that the peak seen in the mass distribution corresponding to symmetric breakup of the system disappeared when the results were corrected for secondary emissions [1,2]. These emissions can also have a strong influence on the average total kinetic energies observed for the fragments. Although the average velocity of the fragments in a given breakup channel will not change, under reasonable assumptions of the decay process, these fragments will be identified as corresponding to a lower charge or lower mass channel, where a different average velocity might pertain for particles which do not undergo secondary evaporation. The net result can be a measured total kinetic energy for a mass channel which is different from what would have been observed in the absence of this evaporation. Whether the observed kinetic energy in a channel will be increased or decreased by the secondary emissions is determined by the relative probability of emission to or from that channel.

In order to compare more realistically the transition-state calculations to the experimental results in a number of systems, the effect of secondary light-particle emission was simulated using the binary-decay option of the Monte Carlo evaporation code LILITA [14]. For these calculations the transition-state model was used to determine the primary (preevaporation) mass distribution and mean kinetic energies $\langle E_K^{\rm tot}(Z,A)\rangle$ for the different fragment channels. A Gaussian spread was assumed for these energies with $\sigma(E_K^{\rm tot}(Z,A))/\langle E_K^{\rm tot}(Z,A)\rangle=0.21$. The total excitation energy was assumed to be split between the fragments proportional to their masses. The spin transferred to the fragments was again estimated using the double-spheroid approximation.

From these calculations it was possible to deduce velocity spectra (which could be converted to energy spectra) for the final fragments. These spectra were accumulated for all possible final nuclear charges and nuclear masses, separately, and for laboratory angles between 0° and 40°, binned every 1°. The final isotopic distribution was also determined.

In general, the role of secondary emission for the reactions considered in this paper was found to increase with compound-nucleus mass. For the lighter systems, where secondary emissions were less prevalent, the principal effect of these emissions on the kinetic-energy distributions was to change the shape without strongly modifying the energy corresponding the peak of these distributions. For the heaviest system considered ($^{40}Ca+^{40}Ca$), the emissions lead to a significant change in both the average and peak kinetic energy calculated for a given mass channel from before to after the emissions.

V. COMPARISONS WITH EXPERIMENTAL RESULTS

A. $^{28}Si+^{12}C$ and $^{24}Mg+^{16}O$

The lightest system considered for this paper was ^{40}Ca. Fissionlike yields have been observed for this compound nucleus as populated through the $^{28}Si+^{12}C$ and $^{24}Mg+^{16}O$ reactions. As previously indicated, these yields have been suggested to arise from a dinucleus orbiting mechanism which does not involve the formation of an equilibrated compound nucleus. Since many of the features of orbiting yields are similar to that expected for the fusion-fission mechanism, however, it is interesting to explore the extent to which they can be explained by this latter mechanism.

Figure 4 summarizes some of the experimental results for the $^{28}Si+^{12}C$ system [9,31]. The solid curves are the results of the transition-state calculation discussed in the previous section. It should be emphasized that there are *no* additional parameters for these calculations beyond those discussed in the previous section—the calculations shown by the solid curves have *not* been adjusted for this specific system. The top portion of the figure shows the cross sections measured for evaporation residues and carbon, oxygen, and nitrogen decay channels. (The Monte Carlo simulations of secondary light-particle emissions indicates that this process does not strongly affect either the mass distributions or average fragment energies for this system.) For comparison with the evaporation-

residue yields, the calculated results are shown for both the total fusion cross section (solid line) and this cross section with the fission component subtracted out (dashed line). The arrow at the top of the figure indicates the energy at which incomplete-fusion processes are expected to start becoming significant based on the systematics of Morgenstern *et al.* [34] (this occurs when the velocity of the light reaction partner $v_L/c \cong 0.06$). Up to this point there is good agreement between the calculated and measured evaporation-residue yields.

The cross sections in the oxygen and nitrogen channels are well reproduced by the transition-state model, but significant differences are seen for the carbon channel where the observed cross sections are underpredicted by a factor of 2.5–3. To achieve agreement with the observations, it was found necessary to decrease the fission barrier in the carbon channel. This is seen by the short-dashed curves which correspond to a decrease in the assumed barrier for the carbon channel by 3.0 MeV. (The oxygen and nitrogen channels are also affected by this change, but to a lesser extent as seen in Fig. 4.) Such a shift could result from microscopic shell corrections at the asymmetric saddle point corresponding to the ^{12}C channel. With this correction the predicted cross sections are in good agreement with the experimental values.

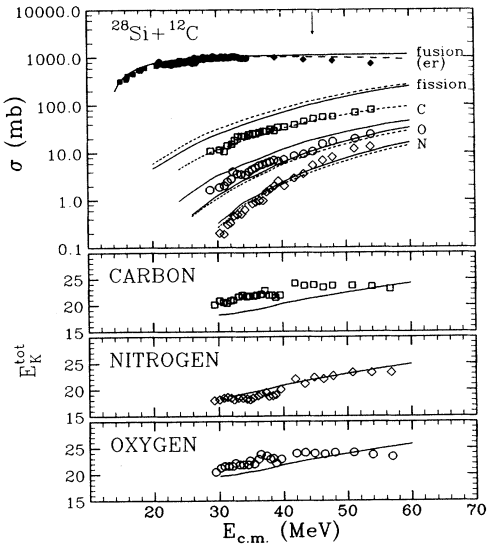

FIG. 4. Comparison of the fusion-fission model calculations to experimental results in the $^{28}Si+^{12}C$ system. The top panel shows the experimental cross sections for evaporation-residue yields [from Refs. [49] (squares), [50] (circles), and [13] (diamonds)] and energy-damped carbon, oxygen, and nitrogen yields [9,28]. The solid curves are the corresponding calculated cross sections based on the transition-state model. The total calculated fission cross sections are also indicated. To compare with the experimental evaporation-residue yields, both the calculated total-fusion cross sections (solid curve) and evaporation cross sections (long-dashed curve) are shown. The short-dashed lines are the result of a 3.0-MeV adjustment to the carbon barrier energy, as discussed in the text. The arrow at the top of the figure indicates the energy at which incomplete-fusion processes are expected to become significant. The bottom three panels show the experimental total kinetic energies [9,28,51] in the three channels (points) as well as the calculated values (lines) using the model discussed in the text.

It is also possible to compare the calculated total kinetic energies in the exit channels with the experimentally determined values. The results for the nitrogen and oxygen channels, also shown in Fig. 4, are again in good agreement with the experimental values. The calculations tend to predict *lower* energies than observed in the carbon channel, however, suggesting that these fragments are emitted either from a more compact configuration than expected for the saddle point or from a higher spin configuration. The change in spin value needed to account for the difference of about 2.7 MeV between the observed and measured total kinetic energies for the ^{12}C channel at $E_{c.m.} = 34.5$ MeV is about $4\hbar$ units, a relatively large value.

Other experimental observations concerning observed "orbiting" yields are also not readily explained within the transition-state model. In particular, the measured spin distributions of the fragments [35], the observation of an entrance-channel dependence for the final fragment mass distributions [36], and the selective population of natural-parity transitions of final fragment states [37] have been used to argue that the orbiting process is distinct from compound-nucleus formation and fission decay. These features have been predominantly observed at lower Q values, however, and it is possible that the orbiting and fusion-fission processes coexist in this mass range.

In the study by Ray *et al.* [36], where the entrance-channel dependence of the "orbiting" yields is explored, it is found that the ratios of the fully energy-damped oxygen to carbon yields are quite different for the $^{24}Mg+^{16}O$ ($E_{c.m.} = 31.8$ MeV) and $^{28}Si+^{12}C$ ($E_{c.m.} = 34.5$ MeV) reactions, even though the measurements are at energies which should form the common ^{40}Ca compound nuclei at a similar excitation energy ($E_x \cong 47.9$ MeV). This ratio is shown in Fig. 5(a) as a function of the mutual fragment excitation energy for the two reactions. The horizontal line is the predicted ratio based on the transition-state model—the model predicts essentially the same ratio for the two reactions. Although an adjustment of the ^{12}C barrier height will bring the predicted ratio into agreement with the $^{28}Si+^{12}C$ reaction results, this clearly does not explain the $^{24}Mg+^{16}O$ results. The dominance of the ^{16}O channel for the more symmetric entrance channel is strongly at odds with the transition-state picture.

It is found, however, that the greatest discrepancy occurs at the lower excitation energies. The regions of excitation energy where the carbon and oxygen fission-fragment yields are expected to be maximum based on the double-spheroid model are indicated by the short lines at the bottom of Fig. 5. At these energies there is better agreement between theory and experiment. This is seen more clearly in Fig. 5(b) where the cross sections for the two channels are shown for the $^{24}Mg+^{16}O$ reaction. (These cross sections were obtained from the angular distribution data of Ref. [36] by extrapolating a $1/\sin\theta$ behavior to the full angular range.) The open histograms show the experimental yields for both the full Q-value

range and for Q values < -8.5 MeV. To the right of the figure, also indicated by an open bar, is the measured evaporation-residue yield [38]. The solid bars are the results of the transition-state calculation using the critical angular momentum for fusion derived from the critical-distance model (with $\sigma_{\rm fus}^{\rm tot}=1006$ mb). Also shown, by the crosshatched bars, are the transition-state calculations performed for a total fusion cross section ($\sigma_{\rm fus}^{\rm tot}=1100$ mb) that leads to better agreement with the measured evaporation-residue yields. It is apparent that a significant part of the cross section at those Q values where fission is expected to be present can be accounted for by this process. A comparison of the solid and crosshatched histograms indicate the sensitivity of the predicted fission yields to the assumed fusion cross section.

The results in the ^{28}Si+^{12}C and ^{24}Mg+^{16}O systems suggest that a simple fusion-fission mechanism cannot be used to fully explain the observed binary yields. It is likely, however, that the more strongly damped of these yields arise, at least in part, from this mechanism. It should be noted that both the ^{28}Si+^{12}C and ^{24}Mg+^{16}O reactions have been shown to demonstrate strong resonant behavior at back angles [39,40]. Also, the ^{24}Mg(^{16}O,^{12}C)^{28}Si reaction demonstrates strong resonant behavior at all angles and to quite large excitation energies [41]. Fusion-fission, orbiting and molecular-resonance behavior all seem to coexist in the large-angle yields for these systems, although how they are related is still unclear.

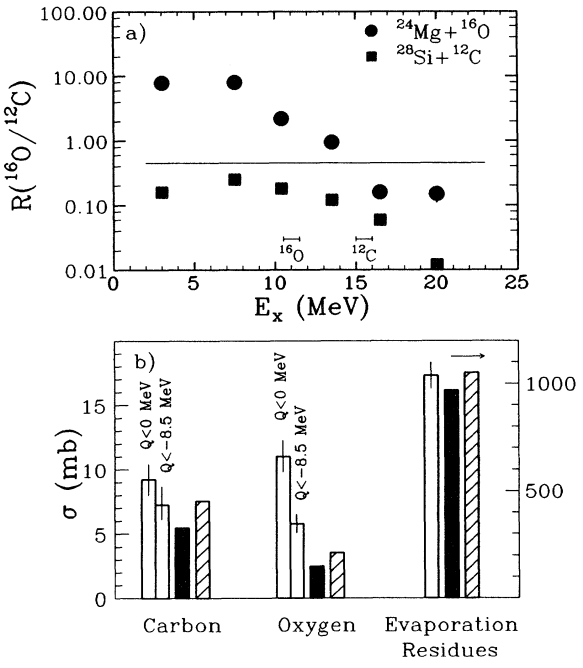

FIG. 5. (a) Ratio of the ^{16}O to ^{12}C orbiting yields as a function of the mutual excitation energy in the exit channel for the ^{24}Mg+^{16}O reaction at $E_{\rm c.m.}=31.8$ MeV [36] and the ^{28}Si+^{12}C reaction at $E_{\rm c.m.}=34.5$ MeV [9]. (b) Angle-integrated carbon, oxygen, and evaporation-residue [38] cross sections for the ^{24}Mg+^{16}O reaction (open bars). The solid bars are the corresponding cross sections using the model discussed in the text, while the crosshatched bars indicate a calculation where the critical angular momentum for fusion is adjusted so as to obtain better agreement between the calculated and experimental evaporation-residue cross sections.

B. ^{28}Si+^{14}N

The observation that at least a component of the large-angle yields for the ^{28}Si+^{12}C and ^{24}Mg+^{16}O reactions cannot be explained by a simple fusion-fission picture makes the ^{28}Si+^{14}N reaction study particularly interesting. Unlike the lighter, even-even, $N=Z$ systems, which reach the ^{40}Ca compound nucleus, there is little, if any, evidence for molecular-resonance behavior in the only slightly heavier ^{28}Si+^{14}N system. It would therefore be expected that the fusion-fission calculations should work better in this system.

This expectation is realized as seen in Fig. 6. The crosshatched bars are the experimentally measured yields of Shivakumar *et al.* [31] for the ^{28}Si+^{14}N reaction at $E_{\rm c.m.}=40$ MeV. The shaded and solid bars are the corresponding calculated yields based on the fusion-fission model before and after the correction for secondary light-particle decay, respectively. The model calculation is found to reproduce the overall experimental behavior quite well, particularly considering the very simple way that shell effects are introduced. The inset shows the average total kinetic energies measured for the stronger channels (points). Again, these results are well reproduced by the model calculations (solid line). (The calculated kinetic energies before secondary light-particle decay are shown. The LILITA calculations indicate that secondary emissions should result in measured kinetic energies being about 1 MeV less than the indicated theoreti-

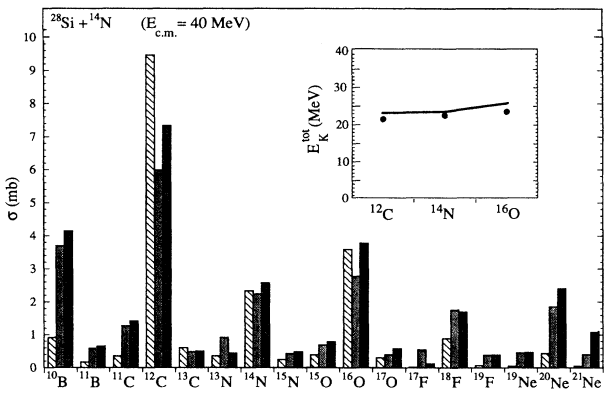

FIG. 6 Cross sections for the binary-decay channels of the ^{28}Si+^{14}N reaction at $E_{\rm c.m.}=40$ MeV. The crosshatched bars are the experiment results of Shivakumar *et al.* [31]. The shaded (solid) bars indicate the calculated cross sections before (after) secondary light-fragment emission using the fusion-fission model discussed in the text. The measured (data points) and calculated (solid line) total-kinetic-energy values for the three strongest channels are shown in the insert.

cal values for each of these three channels, resulting in better agreement with experiment.) Overall, the fusion-fission model seems capable of fully describing the damped binary cross sections for this reaction.

C. $^{35}Cl+^{12}C$ and $^{23}Na+^{24}Mg$

The $^{35}Cl+^{12}C$ and $^{23}Na+^{24}Mg$ reactions have been studied by Beck *et al.* [4,5] and Djerroud *et al.* [6], respectively. These two systems, of quite different mass asymmetry, both populate the ^{47}V compound nucleus. Because of the fewer number of shell-favored channels available for the odd-mass ^{47}V decay, the resulting fission yields might be expected to be spread among a larger number of channels than would be the case for an even-even system.

The open histograms in Fig. 7 show the experimental cross sections for the $^{35}Cl+^{12}C$ reaction at $E_{c.m.}=51.1$ MeV and the $^{23}Na+^{24}Mg$ reaction at $E_{c.m.}=45.5$ MeV. For both measurements the nuclear charge of the fragments was identified. At these energies both reactions populate the ^{47}V compound nucleus at an excitation energy of $E_x=64$ MeV. The results of the transition-state calculations using total fusion cross sections derived from the critical-distance model are shown by the negatively sloped crosshatch histograms. These calculations tend to overpredict the fission cross sections for the $^{35}Cl+^{12}C$ reaction by a factor of 2–3 and underpredict the $^{23}Na+^{24}Mg$ fission cross sections by a similar amount. It can be noted, however, that the predicted evaporation-residue cross sections, also shown in Fig. 7, are also over- and underpredicted for the two reactions, respectively. A summary of these calculations, as well as the other calculations presented in this paper, is given in Table III. This table also includes the calculated cross sections for the ^{8}Be channel for the respective systems. The calculated ^{8}Be cross sections are not shown in Fig. 7 for reasons of scale and the lack of corresponding experimental values (^{8}Be is particle unbound in its ground state).

In order to explore the sensitivity of the calculations to the assumed total fusion cross sections, fission calculations were also performed using critical angular momenta for fusion in the two systems that lead to better agreement of the calculated and experimental evaporation-residue cross sections. These results are shown by the shaded histograms. Correcting the calculated cross sections for secondary light-particle evaporation leads to the solid-filled histograms. The new, light-particle-corrected cross sections are clearly in much better agreement with the experimental values. By further increasing the critical angular momentum for fusion for the $^{23}Na+^{24}Mg$ calculations in order to optimize the agreement between the calculated (corrected for light-particle emission) and experimental fission cross sections, one obtains the positively sloped crosshatch bars. The resulting estimate for the total evaporation-residue yield is still within the uncertainty range of the measured value.

In general, the experimental cross sections for the fully damped binary fragments in these two systems are in excellent agreement with the expectations of the transition-state model. The data indicate, however, the difficulty of

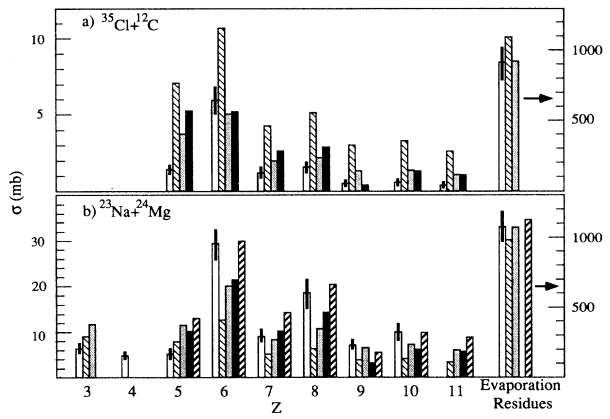

FIG. 7. Fissionlike the evaporation-residue cross sections for the (a) $^{35}Cl+^{12}C$ reaction at $E_{c.m.}=51.1$ MeV [5] and the (b) $^{23}Na+^{24}Mg$ reaction at $E_{c.m.}=45.5$ MeV [6]. The experimental values are shown by the open bars with uncertainties indicated. The negatively sloped stripped bars are the results of the fusion-fission calculation. The shaded bars are the results of the fission calculation with the critical angular momentum adjusted to obtain better agreement between the calculated and measured evaporation-residue cross sections. The solid bars are the corresponding cross sections after allowing for secondary light-particle emissions from the fragments. The positively sloped stripped bars for the $^{23}Na+^{24}Mg$ reaction show a calculation where the critical angular momentum for fusion has been adjusted to improve the agreement between the calculated and experimental fission yields.

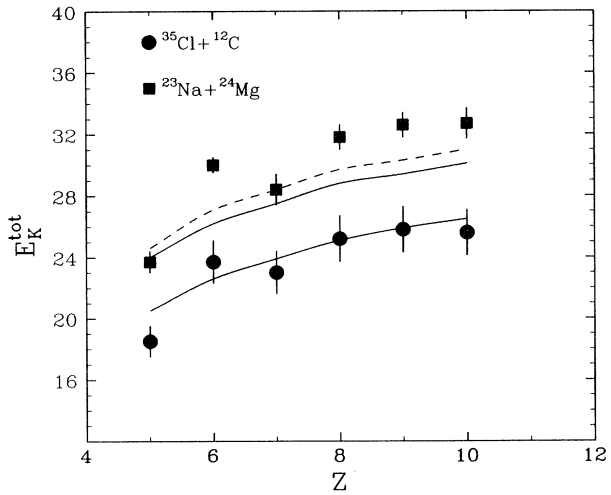

FIG. 8. Total fragment kinetic energies observed for the $^{35}Cl+^{12}C$ reaction at $E_{c.m.}=51.1$ MeV (circles) [5] and the $^{23}Na+^{24}Mg$ reaction at $E_{c.m.}=45.5$ MeV (squares) [6]. The solid curves are the results of the calculation discussed in the text. The dashed curve corresponds to the calculations where the critical angular momentum for fusion has been adjusted to improve the agreement between the calculated and experimental fission yields for the $^{23}Na+^{24}Mg$ system.

TABLE III. Summary of fusion-fission calculations discussed in text. The calculations labeled "critical distance" use the critical angular momentum for fusion determined by the critical-distance model discussed in the text.

Reaction	$E_{c.m.}$ (MeV)	Fusion calculation	l_0	l_{Sierk}	σ_{fus}^{tot} (mb)	σ_{ER} (mb)	σ_{fis} (mb)	$\sigma(^8Be)$ (mb)
$^{28}Si+^{12}C$	34.5	critical distance	$21.2\hbar$	$29.9\hbar$	1065	1026	39	21
$^{24}Mg+^{16}O$	31.8	critical distance	20.6		1006	969	37	19
		fit ER	22.1		1100	1051	49	26
$^{28}Si+^{14}N$	40.0	critical distance	23.7	33.4	1072	1015	57	20
$^{35}Cl+^{12}C$	51.1	critical distance	28.0	39.0	1167	1088	79	28
		fit ER	25.4		964	922	42	15
$^{23}Na+^{24}Mg$	45.5	critical distance	28.5	39.0	1069	983	83	31
		fit ER	30.8		1200	1069	131	45
		fit fission	32.1		1300	1123	177	58
$^{32}S+^{24}Mg$	51.6	critical distance	31.7	43.5	961	919	42	20
	60.5	critical distance	35.6		1058	936	122	39
$^{40}Ca+^{40}Ca$	98.5	critical distance	53.8	56.1	999	750	249	19
	115.5	critical distance	62.9		1164	669	495	14
		$l_0=l_{Sierk}$	56.1		930	646	284	17
$^{28}Si+^{50}Cr$	96.2	critical distance	53.9	57.3	1148	910	238	23

making *a priori* estimates of fission cross sections without prior knowledge of the total fusion (or evaporation residue) cross sections. In this case, the critical-distance model predicted the more asymmetric-mass entrance channel to have the greater total fusion cross section, in contradiction to experiment.

The final fragment total kinetic energies observed for the two reactions are shown in Fig. 8. The calculated energies are in excellent agreement for the $^{35}Cl+^{12}C$ system (lower solid curve), although the predicted energies are about 2–3 MeV too low for the $^{23}Na+^{24}Mg$ system. For comparison with the $^{23}Na+^{24}Mg$ system, both the calculation that leads to agreement with the observed evaporation-residue cross sections (upper solid curve) and the calculation leading to better agreement with the fission cross sections (dashed curve) are shown.

Secondary light-particle evaporation in these systems is seen to have a small effect on the observed charge distributions. These emissions also affect the observed total-kinetic-energy distributions. The Monte Carlo simulations systems suggest that, for these systems, the average energies are shifted more than the peak positions as the shape of the distributions become skewed, with shifts on the order of 1–3 MeV for the average energies and lesser amounts for the peak energies. Since these shifts are still relatively small, the preevaporation (approximating the peak post-evaporation) energies are shown in Fig. 8.

D. $^{32}S+^{24}Mg$

The damped binary yields for the $^{32}S+^{24}Mg$ reaction at $E_{c.m.}=51.6$ and 60.5 MeV have been shown previously to be well reproduced by the transition-state model [2]. The measurement of these cross sections was done using a coincidence technique that allowed for the primary, preevaporation mass distribution to be deduced. The experimental method and associated analysis are discussed in Refs. [1] and [2].

Figure 9 shows that primary mass distribution deduced from this experiment by the open histograms. For the lower-energy data the cross sections have been binned every two masses, while every mass is shown for the higher energy. The crosshatched histograms show the results of the present calculation using the critical-distance model to deduce the total fusion cross sections. These are the predicted, preevaporation cross sections since the experimental results already take into account the secon-

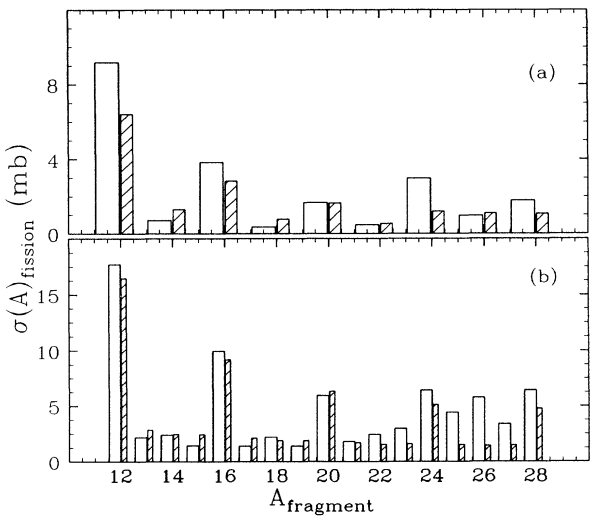

FIG. 9. Experimental (open bars) [1,2] and calculated (striped bars) mass distributions for the $^{32}S+^{24}Mg$ reaction at (a) $E_{c.m.}=51.6$ MeV and (b) $E_{c.m.}=60.5$ MeV. The experimental distributions have been corrected for secondary light-particle emission using coincidence data, as discussed in Ref. [2].

dary emission of light particles. Good agreement is achieved between the calculated and experimental yields. The total evaporation-residue cross sections predicted at $E_{c.m.} = 51.6$ and 60.5 MeV are 919 and 936 mb, respectively, to be compared to the experimental values of 1080 ± 130 and 1050 ± 100 mb [2]. The small increase in the fusion critical angular momentum needed to bring the evaporation-residue yields into better agreement with experiment also improves the overall agreement of the fission cross sections.

In the previous analysis of these data, similar results were achieved, but using different level-density parameters for the evaporation residues and fission channels, with $a_f/a_n = 0.86$. The principal change in the present calculations, where these two parameters are set (approximately) equal [42], is the more consistent treatment of the level densities. The present calculation uses the same level-density expression for the saddle point and for the evaporation-residue channels—in the previous analysis these two expressions were different. Also, the present calculation consistently uses the yrast energies calculated with the finite-range model in deriving residue level densities.

The total kinetic energies observed in the strongest mass channels at the two energies are shown in Fig. 10 along with the calculated energies based on the double-spheroid approximation. Good agreement is achieved for the more symmetric-mass exit channels, although a 2–3-MeV overestimate of these energies is seen for the more asymmetric-mass channels. Increasing the assumed critical angular momentum for fusion to better reproduce the evaporation-residue and fission yields can only increase this discrepancy. This result suggests the possibility that post-saddle damping of the relative motion might be greater for asymmetric fission than for symmetric fission.

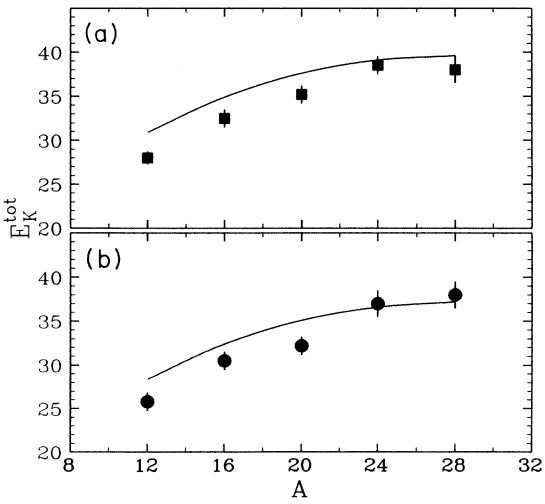

FIG. 10. Fragment total kinetic energies for the $^{32}S + ^{24}Mg$ reaction at (a) $E_{c.m.} = 51.6$ MeV and (b) $E_{c.m.} = 60.5$ MeV [2]. The curves show the results of the calculation discussed in the text.

E. $^{40}Ca + ^{40}Ca$ and $^{50}Cr + ^{28}Si$

Studies of the fissionlike yields from the $^{40}Ca + ^{40}Ca$ reaction at $E_{c.m.} = 98.5$ and 115.5 MeV [24,43] indicate that this system is above the Businaro-Gallone point [44] marking the transition from asymmetric to symmetric fission. The experimental mass distributions at the two energies are shown in Fig. 11. The data points and associated uncertainties were deduced from the angular distribution data of Ref. [24] by extrapolating these distributions over the full angular range assuming a $1/\sin\theta$ angular dependence. At both energies the experimental distributions show maxima near to, but shifted slightly down from, the symmetric breakup mass of $A = 40$.

The mass-asymmetry-dependent fission barriers of the ^{80}Zr compound nucleus undergo a transition at high spins, as seen in Fig. 2. At a spin value of $J = 36\hbar$ ($0.64 J_{max}$), the saddle-point energy is found to favor asymmetric breakup of the system, as is the case for the lighter systems considered. However, at the higher spin of $J = 54\hbar$ ($0.92 J_{max}$), a very different behavior is observed with symmetric fission being favored. The peak of the fission spin distributions at 98.5 and 115.5 MeV are found to be near $50\hbar$ and $56\hbar$, respectively, from the transition-state calculations using the critical angular momentum for fusion of the critical-distance model. Symmetric-mass fission is expected in this spin region as shown by the calculated distributions in Fig. 11 (bold-line histogram). As expected from the saddle-point behavior, the predicted mass distribution at the lower energy is somewhat broader, following from the flatter mass depen-

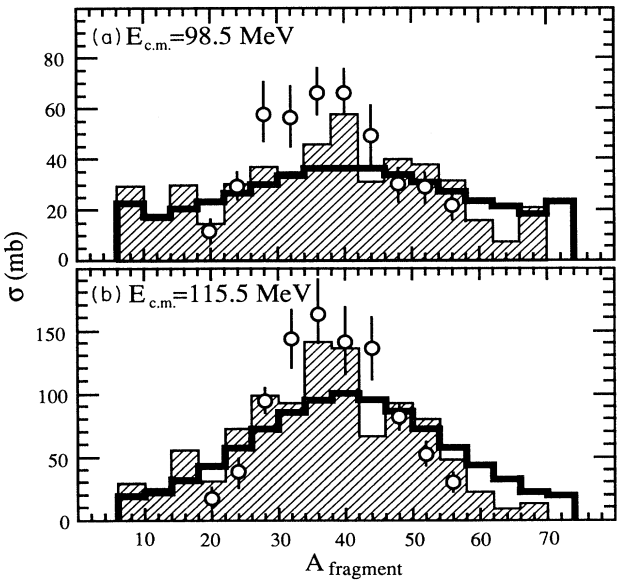

FIG. 11. Experimental (data points) and calculated (histograms) mass distributions for the $^{40}Ca + ^{40}Ca$ reaction at (a) $E_{c.m.} = 98.5$ MeV and (b) $E_{c.m.} = 115.5$ MeV [24]. The calculated distributions before (broad line) and after (crosshatched) the emission of secondary light particles are shown.

dence of the saddle-point energies at the lower spin. The predicted mass distributions following light-particle emissions from the fragments are also shown in Fig. 11 (shaded region), with the results found to be in good agreement with the experimental results.

The total kinetic energies of the fragments observed at the two energies are also in good agreement with the double-spheroid calculations. This is seen in Fig. 12 where these energies are shown for a number of mass channels. For both energies the thin curves at somewhat higher energies than the experimental values show the predicted kinetic energies in the absence of secondary light-particle emissions. The darker curves are the corresponding energies after the secondary evaporation process. For this system the secondary evaporations are found to significantly change the predicted energies. Close inspection reveals that there is still a tendency to overpredict the energies in the more asymmetric-mass channels, as was found in the $^{32}S+^{24}Mg$ case. This again could indicate a post-saddle damping in the fission process that is asymmetry dependent.

Although the mass and total-kinetic-energy distributions for the $^{40}Ca+^{40}Ca$ reaction are found to be well described by the transition-state model, there is a question concerning the evaporation-residue yields. The calculated total fusion cross sections at 98.5 and 115.5 MeV are 999 and 1164 mb, respectively, with corresponding evaporation-residue cross sections of 750 and 669 mb. Experimental cross sections are not available at these two energies, but the measurements of Doubre *et al.* [45], which extend up to $E_{c.m.}=97.5$ MeV and include a value at 115 MeV, suggest that cross sections closer to 1000 mb might be expected, at least at 98.5 MeV. It is possible that more mass-asymmetric fission channels could have influenced the earlier evaporation-residue measurements,

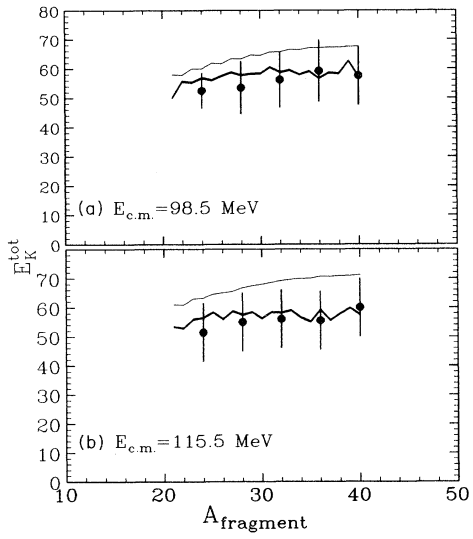

FIG. 12. Fragments total kinetic energies for the $^{40}Ca+^{40}Ca$ reaction at (a) $E_{c.m.}=98.5$ MeV and (b) $E_{c.m.}=115.5$ MeV [24]. The thin and thick lines show the calculated values before and after secondary light-particle emission, respectively.

but this needs to be demonstrated with a self-consistent measurement of the evaporation-residue and fission cross sections.

Another question raised by these calculations, already noted by Evans *et al.* [24], concerns the consistency of the critical angular momentum value needed to explain the observed evaporation-residue and fission yields at the higher bombarding energy and the Sierk value for the limiting angular momentum for stability against symmetric fission of the ^{80}Zr composite system. These two values are tabulated in Table III. Using the Sierk value for the fusion critical angular momentum results in a prediction of significantly less fission yield than observed. It is possible that the higher fission barriers corresponding to the more asymmetric saddle-point configurations may influence the stability of the compound nucleus, but this point requires further study.

In addition to studying the $^{40}Ca+^{40}Ca$ fissionlike yields, Evans *et al.* [24,43] have also looked at these yields as produced in the $^{28}Si+^{50}Cr$ reaction. The resulting mass distributions were found to be strikingly different. Figure 13 shows the experimental center-of-mass differential cross sections for the $^{40}Ca+^{40}Ca$ reaction at $E_{c.m.}=98.5$ MeV and $\theta_{lab}=20°$ compared to the cross sections for the $^{28}Si+^{50}Cr$ system at $E_{c.m.}=96.2$ MeV and $\theta_{lab}=30°$. The strong maximum seen for the symmetric breakup of the $^{40}Ca+^{40}Ca$ systems is missing from the $^{28}Si+^{50}Cr$ data. Evans *et al.* argue that this is unlikely to be a consequence of the Businaro-Gallone transition since these two systems have very similar fissil-

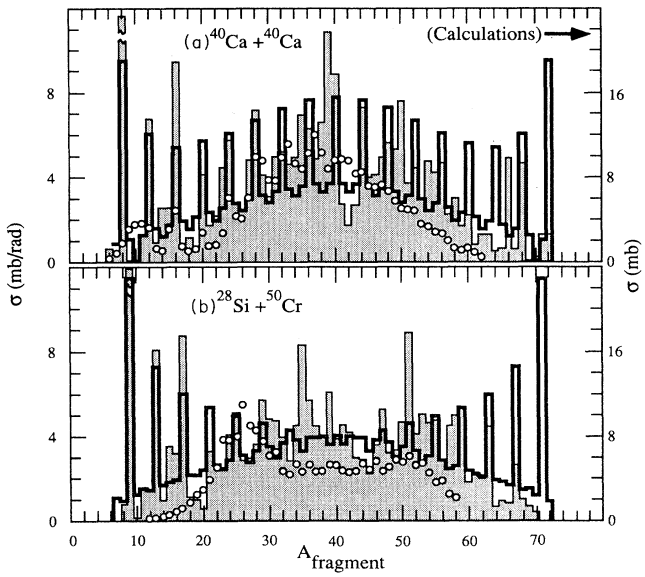

FIG. 13. Differential center-of-mass cross sections (points) as a function of fragment mass for the (a) $^{40}Ca+^{40}Ca$ reaction at $E_{c.m.}=98.5$ MeV and $\theta_{lab}=20°$ [24] and the (b) $^{28}Si+^{50}Cr$ reaction at $E_{c.m.}=96.2$ MeV and $\theta_{lab}=30°$ [43]. The thick-line and shaded histograms show the calculated total (angle-integrated) cross sections before and after secondary light-particle emission, respectively.

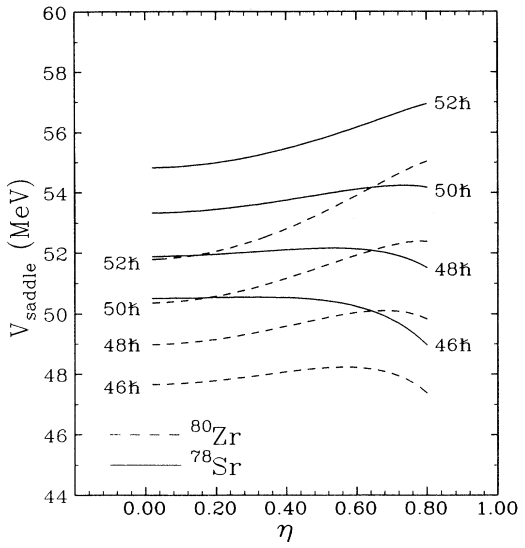

FIG. 14. Spin- and mass-asymmetry-dependent saddle-point energies for the ^{78}Sr (solid lines) and ^{80}Zr (dashed lines) compound nuclei. The barrier energies are shown for spins $46\hbar$, $48\hbar$, $50\hbar$, and $52\hbar$.

ity parameters, and the critical angular momenta for fusion are also expected to be very similar. The possibility of a fast-fission mechanism accounting for the asymmetry dependence of the ^{28}Si+^{50}Cr yields is suggested.

With the suggestion of a new reaction mechanism being observed in this mass region, it is interesting to compare the predictions of the present calculation with the experimental results. The bold-line histograms in Fig. 13 are the primary (preevaporation) mass distributions predicted for the two systems using the critical-distance model to deduce the total fusion cross sections. The total channel cross sections (angle integrated) are shown. The shaded regions show the predicted mass distributions following light-particle evaporation. It can be noted that quite different mass distributions are predicted for the two reactions, with the ^{28}Si+^{50}Cr system taking on a more asymmetric behavior, as seen experimentally. Although the calculations suggest similar angular momenta values are involved in the fission process ($\langle l_{fis} \rangle \cong 50\hbar$) for both systems, as suggested by Evans *et al.*, the corresponding saddle-point energies show a subtle difference. This is seen in Fig. 14 where these energies are shown as functions of the mass asymmetry for spin values $46\hbar$, $48\hbar$, $50\hbar$, and $52\hbar$ for both systems. The ^{28}Si+^{50}Cr system is seen to be just crossing the Businaro-Gallone point in this spin region, whereas the ^{40}Ca+^{40}Ca system favors symmetric fission throughout the region. Although it is not clear whether this transition behavior can fully explain the experimental results seen in Fig. 13, it does suggest that at least part of differences in the observed mass dependence might arise from this cause.

VI. SUMMARY AND CONCLUSIONS

Fissionlike cross sections have been observed for a large number of light heavy-ion systems by a number of different investigators. Explanations for these yields have varied from heavy-ion fusion followed by fission to different deep-inelastic-scattering mechanisms. None of the models have been fully adequate to explain the yields and have been particularly weak in offering a means of *a priori* prediction of the expected cross sections in a given system.

Although the general characteristics of the yields suggest a fusion-fission mechanism, estimates of fission cross sections using the standard, lepodermous liquid-drop model are considerably smaller than the observed values. Also, some of the observed behaviors of the yields in the ^{40}Ca mass region (entrance-channel dependence, spin alignment, etc.) are inconsistent with a compound-nucleus origin.

In this paper a procedure for calculating fission cross sections and fragment total kinetic energies in light systems is developed. The calculations are based on the transition-state model of fission and use saddle-point energies derived from the diffuse-surface, finite-nuclear-range model. A simple parametrization, which can be easily incorporated into the transition-state calculations, is developed for obtaining these saddle-point energies over the mass range $40 \leq A_{CN} \leq 80$. By applying a critical-distance model to deduce the total fusion cross sections, a parameter-free procedure for calculating fission cross sections and fragment energies as a function of fragment mass and charge is developed. These calculations are found to reproduce the overall experimental results quite well.

Since the saddle and scission points in light nuclear systems are similar, it is expected that the results of the transition-state calculations, based on the saddle-point level densities, will be comparable to those of the extended Hauser-Feshbach model [29,30], which uses a product of fragment level densities to determine fission probabilities. The geometry of the transition-state calculations is more fully established, however, being based on the macroscopic energy calculations. Any significant differences that might exist in the model predictions of these two fusion-fission pictures are most likely to be highlighted once more realistic shell corrections are developed for the transition-state calculations and more detailed experimental charge and mass distributions of fission fragments become available.

The question of fission at higher energies in light systems is interesting since this process is found to dominate over light-particle emission in the highest partial waves contributing to fusion. It is unlikely that one can separate the question of what limits fusion in light heavy-ion systems from an understanding of the fission process. Although this paper concentrates on systems where the complete-fusion process is expected to dominate over incomplete-fusion processes, a better understanding of the fission process may suggest future experiments where the competition between complete-fusion-fission and incomplete-fusion processes are explored.

Still unresolved is the question of the orbiting process in lighter systems. Although the fusion-fission picture can explain the more fully damped yields observed in, for example, the ^{28}Si+^{12}C and ^{24}Mg+^{16}O reactions, this

model does not explain some of the other characteristics of these yields, particularly for less negative Q values. It appears that orbiting, molecular resonance, and fission behaviors all coexist in these systems, and their relationships still need to be sorted out.

Finally, it is interesting to ask whether the fission process might extend to even lighter systems than considered here. Szanto de Toledo *et al.* [46] have observed fission-like decay of ^{20}Ne as populated in the ^{10}B+^{10}B reaction. The present calculations were not extended below mass 40 because finite-range model calculations of yrast energies were not available for these lighter systems. It is clearly possible to remove this restriction in the future. Although the use of statistical calculations in systems of so few particles can be questioned, it can be noted that heavy-ion reactions are still able to populate regions of very high level densities.

ACKNOWLEDGMENTS

The author would like to thank F. W. Prosser for his comments on the manuscript. This work has been supported in part by the U.S. Department of Energy, Nuclear Physics Division, under Contract No. DE-FG02-89ER40506. Additional support has come from the University of Kansas General Research Fund and from the University of Kansas New Faculty General Research Program.

[1] S. J. Sanders, D. G. Kovar, B. B. Back, C. Beck, B. K. Dichter, D. Henderson, R. V. F. Janssens, J. G. Keller, S. Kaufman, T.-F. Wang, B. Wilkins, and F. Videback, Phys. Rev. Lett. **59**, 2856 (1987).

[2] S. J. Sanders, D. G. Kovar, B. B. Back, C. Beck, D. J. Henderson, R. V. F. Janssens, T. F. Wang, and B. D. Wilkins, Phys. Rev. C **40**, 2091 (1989).

[3] S. J. Sanders, B. B. Back, R. V. F. Janssens, D. G. Kovar, D. Habs, D. Henderson, T. -L. Khoo, H. Korner, G-E. Rathke, T. F. Wang, F. L. H. Wolfs, and K. B. Beard, Phys. Rev. C **41**, 1901 (1990).

[4] C. Beck, B. Djerroud, B. Heusch, R. Dayras, R. M. Freeman, F. Haas, A. Hachem, J. P. Wieleczko, and M. Youlal, Z. Phys. A **334**, 521 (1989).

[5] C. Beck, B. Djerroud, R. M. Freeman, F. Haas, B. Heusch, A. Morsad, M. Youlal, A. Hachem, R. Dayras, J. P. Wieleczko, T. Matsuse, and S. M. Lee, in *Workshop on the Interface between Nuclear Structure and Heavy-Ion Reaction Dynamics (1990: University of Notre Dame),* edited by R. R. Betts and J. J. Kolata (IOP, Bristol, 1991), p. 213.

[6] B. Djerroud, C. Beck, M. Vuillet-A-Ciles, R. M. Freeman, F. Haas, B. Heusch, A. Morsad, M. Youlal, A. Hachem, and T. Matsuse, in Proceedings of the Varenna Conference, 1991 (in press).

[7] A. Ray, D. Shapira, J. Gomez del Campo, H. J. Kim, C. Beck, B. Djerroud, B. Heusch, D. Blumenthal, and B. Shivakumar, Phys. Rev. C **44**, 514 (1991).

[8] L. G. Moretto, Nucl. Phys. **A247**, 211 (1975).

[9] D. Shapira, R. Novotny, Y. D. Chan, K. A. Erb, J. L. C. Ford, Jr., J. C. Peng, and J. D. Moses, Phys. Lett. **114B**, 111 (1982).

[10] D. Shapira, Phys. Rev. Lett. **61**, 2153 (1988).

[11] R. Vandenbosch and J. R. Huizenga, *Nuclear Fission* (Academic, New York, 1973).

[12] A. J. Sierk, Phys. Rev. C **33**, 2039 (1986).

[13] B. A. Harmon, S. T. Thornton, D. Shapira, J. Gomez del Campo, and M. Beckerman, Phys. Rev. C **34**, 552 (1986).

[14] J. Gomez del Campo, J. A Biggerstaff, R. A. Dayras, D. Shapira, A. H. Snell, P. H. Stelson, and R. G. Stokstad, Phys. Rev. C **29**, 1722 (1984), and references therein.

[15] K. T. R. Davis and J. R. Nix, Phys. Rev. C **14**, 1977 (1976); H. J. Krappe, J. R. Nix, and A. J. Sierk, *ibid.* **20**, 992 (1979); K. T. R. Davis and A. J. Sierk, *ibid.* **31**, 915 (1985).

[16] Computer code BARFIT; see Ref. [12].

[17] J. R. Nix, Nucl. Phys. **A130**, 241 (1969).

[18] A. J. Sierk, Phys. Rev. Lett. **55**, 582 (1985).

[19] H. J. Krappe, J. R. Nix, and A. J. Sierk, Phys. Rev. C **20**, 992 (1979).

[20] R. Bass, *Nuclear Reactions with Heavy Ions* (Springer-Verlag, Berlin, 1980).

[21] P. Möller and J. R. Nix, At. Data Nucl. Data Tables **26**, 165 (1981).

[22] K. T. R. Davies, R. A. Managan, J. R. Nix, and A. J. Sierk, Phys. Rev. C **16**, 1890 (1977).

[23] F. Pühlhofer, Nucl. Phys. **A280**, 267 (1977).

[24] P. M. Evans, A. E. Smith, C. N. Pass, L. Stuttgé, B. B. Back, R. R Betts, B. K. Dichter, D. J. Henderson, S. J. Sanders, F. Videbaek, and D. B. Wilkins, Nucl. Phys. **A526**, 365 (1991).

[25] T. D. Thomas, Nucl. Phys. **53**, 577 (1964).

[26] A. Bohr and B. R. Mottelson, *Nuclear Structure* (Benjamin, New York, 1969), Vol. 1.

[27] B. Shivakumar, D. Shapira, P. H. Stelson, M. Beckerman, B. A. Harmon, K. Teh, and D. A. Bromley, Phys. Rev. Lett. **57**, 1211 (1986).

[28] B. Shivakumar, S. Ayik, B. A. Harmon, and D. Shapira, Phys. Rev. C **35**, 1730 (1987).

[29] T. Matsuse and S. M. Lee, in *Proceedings of the International Symposium on Developments of Nuclear Cluster Dynamics, Sapporo, Japan,* edited by Y. Akaishi, K. Katō, H. Noto, and S. Okabe (World Scientific, Singapore, 1989), p. 312.

[30] S. M. Lee, W. Yokota, and T. Matsuse, in *Proceedings of the Symposium on the Many Facets of Heavy-Ion Fusion Reactions, Argonne 1986,* Report No. ANL-PHY-86-1, 1986, p. 63.

[31] B. Shivakumar, D. Shapira, P. H. Stelson, S. Ayik, B. A. Harmon, K. Teh, and D. A. Bromley, Phys. Rev. C **37**, 652 (1988).

[32] S. Ayik, D. Shapira, and B. Shivakumar, Phys. Rev. C **38**, 2610 (1988).

[33] B. D. Wilkins, E. P. Steinberg, and R. R. Chasman, Phys. Rev. C **14**, 1832 (1976).

[34] H. Morgenstern, W. Bohne, W. Galster, and K. Brabisch, Phys. Rev. Lett. **52**, 1104 (1984).

[35] A. Ray, D. Shapira, M. L. Halbert, J. Gomez del Campo, H. J. Kim, J. P. Sullivan, B. Shivakumar, and J. Mitchell, Phys. Rev. C **43**, 1789 (1991).

[36] A. Ray, S. Gil, M. Khandaker, D. D. Leach, D. K. Lock, and R. Vandenbosch, Phys. Rev. C **31**, 1573 (1985).

[37] W. Dünnweber, A. Glaesner, W. Hering, D. Konnerth, R.

Ritzka, W. Trombik, J. Czakanski, and W. Zipper, Phys. Rev. Lett. **61**, 927 (1988).

[38] S. L. Tabor, D. F. Geesaman, W. Henning, D. G. Kovar, K. E. Rehm, and F. W. Prosser, Jr., Phys. Rev. C **17**, 2136 (1978).

[39] J. Barrette, M. J. LeVine, P. Braun-Munzinger, G. M. Berkowitz, M. Gai, J. W. Harris, C. M. Jachcinski, and C. D. Uhlhorn, Phys. Rev. C **20**, 1759 (1979).

[40] M. Paul, S. J. Sanders, D. F. Geesaman, W. Henning, D. G. Kovar, C. Olmer, J. P. Schiffer, J. Barrette, and M. J. LeVine, Phys. Rev. C **21**, 1802 (1980).

[41] S. J. Sanders, C. Olmer, D. F. Geesaman, W. Henning, D. G. Kovar, M. Paul, and J. P. Schiffer, Phys. Rev. C **22**, 1914 (1980).

[42] With $a_n = A_{ER}/8.0\ \mathrm{MeV}^{-1}$ and $a_f = A_{CN}/8.0\ \mathrm{MeV}^{-1}$.

[43] P. M. Evans, A. E. Smith, C. N. Pass, L. Stuttgé, R. R. Betts, S. J. Sanders, B. B. Back, B. K. Dichter, D. J. Henderson, F. Videbaek, and B. D. Wilkins, Phys. Lett. B **229**, 25 (1989).

[44] U. L. Businaro and S. Gallone, Nuovo Cimento **5**, 315 (1957).

[45] H. Doubre, A. Gamp, J. C. Jacmart, N. Poffé, J. C. Roynette, and J. Wilczyński, Phys. Lett. **73B**, 135 (1978).

[46] A. Szanto de Toledo, M. M. Coimbra, N. Added, R. M. Anjos, N. Carlin Filho, L. Fante, Jr., M. C. S. Figueira, V. Guimarães, and E. M. Szanto, Phys. Rev. Lett. **62**, 1255 (1989).

[47] S. J. Sanders, R. R. Betts, I. Ahmad, K. T. Lesko, S. Saini, B. D. Wilkins, F. Videbaek, and B. K. Dichter, Phys. Rev. C **34**, 1746 (1986).

[48] R. Ritzka, W. Dünnweber, A. Glaesner, W. Hering, H. Puchta, and W. Trautmann, Phys. Rev. C **31**, 133 (1985).

[49] S. Gary and C. Volant, Phys. Rev. C **25**, 1877 (1982).

[50] K. T. Lesko, D. -K. Lock, A. Lazzarini, R. Vandenbosch, V. Metag, and H. Doubre, Phys. Rev. C **25**, 872 (1982).

[51] D. Shapira, D. Schull, J. L. C. Ford, Jr., B. Shivakumar, R. L. Parks, R. A. Cecil, and S. T. Thornton, Phys. Rev. Lett. **53**, 1634 (1984).